Article:
Theobald, DW, Hanson, B orcid.org/0000-0002-1720-1656, Fairweather, M et al. (1 more author) (2020) Implications of hydrodynamics on the design of pulsed sieve-plate extraction columns: A one-fluid multiphase CFD model using the volume of fluid method. Chemical Engineering Science, 221. 115640. ISSN 0009-2509

https://doi.org/10.1016/j.ces.2020.115640

Implications of hydrodynamics on the design of pulsed sieve-plate extraction columns: A one-fluid multiphase CFD model using the volume of fluid method

Daniel W. Theobald*, Bruce Hanson, Michael Fairweather, Peter J. Heggs

School of Chemical and Process Engineering, University of Leeds, Leeds, LS2 9JT

Abstract

Presented is a detailed assessment of dispersive mixing and turbulence characterisation of an industrially representative pulsed sieve-plate extraction column (PSEC) obtained using multiphase CFD modelling. The system consists of a 150 mm diameter column with two perforated plates dispersing a 30 vol% dodecane/tributyl phosphate mixture in 3 M nitric acid. Operational conditions were chosen to examine pseudo steady-state dispersion regime operation. Three-dimensional transient flow calculations were performed using large eddy simulation (LES), coupled with the volume of fluid method. This study finds that LES is effective at capturing the different scales of turbulence present within PSECs, and their operational influence. Explicit analysis of the hydrodynamics established that the sieve-plates drive dispersive mixing through their influence on the resulting turbulent flow and flow structures. Furthermore, the standard round-hole sieve-plate design is found to perform poorly at producing and distributing the types of flow and turbulence beneficial to droplet size reduction.

Keywords: CFD simulation, Volume of fluid, Pulsed sieve-plate extraction column, Dispersive mixing, Liquid-liquid flow, OpenFOAM

1. Introduction

The pulsed sieve-plate extraction column (PSEC) has played a key role in nuclear solvent extraction processes since reprocessing of spent nuclear fuels started more than half a century ago. For sensitive operations involving rich solutions of fissile plutonium, geometrically safe PSECs offered a feasible means of conducting solvent extraction operations by dramatically reducing toxicity, radiological and criticality risks. Since its early adoption into the industry, the PSEC has become a vital component of reprocessing facilities such as Hanford (USA), Idaho National Laboratory (USA), La Hague (France) and the thermal oxide reprocessing plant, THORP, (UK) (McKetta, 1998).

PSECs operate on the principle of facilitating mass transfer through maximising interfacial contact area during counter-current flow between two mixed fluids, a heavy and a light phase. The heavy phase usually consists of a rich aqueous liquor containing the desired components for extraction, with the light organic phase containing a ligand capable of removing the desired components from the aqueous phase. The heavy phase enters from the top section of the column and exits from the bottom. Conversely, the light phase will enter from the bottom and flow from an outlet at the top. Settling sections are located at the top and bottom of the column for the organic and aqueous phases respectively. Pulsing of the light phase fluid is thought to induce shear forces on the fluid across the sieve-plates leading to efficient droplet formation in those regions of high shear (Yadav and Patwardhan, 2008).

Classically, PSECs are sized and built through empirical design correlations and subsequent pilot plant tests. However, from a review of available literature, presented by Yadav and Patwardhan (2008), it is evident that little is known about the underlying fundamental hydrodynamic behaviour of such columns, resulting in a poor design basis. Some resurgence in PSEC research is apparent over the past decade through new investigations into their hydrodynamics using computational fluid dynamics (CFD). However, these studies are mainly rudimentary, typically employing Reynolds-averaged Navier-Stokes (RANS) methods using k-ε turbulence modelling to close the descriptive equations

*Corresponding Author

Email address: pm11dt@leeds.ac.uk (Daniel W. Theobald)

Nomenclature

α	Local volume fraction in VOF
$\Delta\rho$	Density difference between phases (kgm^{-3})
Δ	Filtered length scale (m)
λ_0	Kolmogorov length scale (m)
λ_{MI}	Mixing index
μ_c, μ_d	Continuous/dispersed phase dynamic viscosity (Pa·s)
ν	Kinematic viscosity (m^2s^{-1})
ν_t	Sub grid scale kinematic turbulence eddy viscosity
Ω	Vorticity tensor (s^{-1})
ϕ_f	Mesh cell face volumetric flux
ρ	Density of fluid (kgm^{-3})
ρ'	Fluctuation in local density (kg/m^{-3})
ρ_c, ρ_d	Continuous/dispersed phase density (kgm^{-3})
σ	Interfacial tension (Nm)
τ^R	Residual stress tensor
τ^t	Turbulent (Reynolds) stress tensor (Pa)
τ^v	Viscous stress tensor (Pa)
T	Lagrangian relaxation time scale
ε	Dissipation rate of turbulence kinetic energy (m^2s^{-3})
A	Amplitude of pulse (m)
D	Column diameter (m)
d	Plate hole diameter (m)
e	Fractional free area
f	Frequency of pulse (Hz)
G	Filter function
g	Gravitational acceleration (ms^{-1})
h	Plate spacing (m)
k	Turbulence kinetic energy (m^2s^{-2})
L	Leonard stress tensor
M	Scaled composite rate-of-strain tensor
n^f	Mesh face centred interface normal vector
P	Pressure (Pa)
R	Insphere radius of tetrahedron (m)
S	Rate-of-strain tensor (s^{-1})
s^f	Mesh cell face area vector
T	Double filtered residual stress tensor
U	Velocity (ms^{-1})
u'	Residual velocity field (ms^{-1})
U^r	Relative artificial compression velocity in VOF
U_c, U_d	Continuous and dispersed phase superficial velocity (ms^{-1})
V_C	Mesh cell volume (m^3)

(Yadav and Patwardhan, 2009; Kolhe et al., 2011; Sen et al., 2018). Whether this approach can be considered suitable for systems of such complexity is questionable. In particular, it is likely that the time-dependent nature of a pseudo-steady-state, three-dimensional, countercurrent, liquid-liquid system cannot be realistically represented through eddy-viscosity based turbulence modelling.

This work aims to improve on previous PSEC modelling efforts moving away from time-averaged modelling approaches in order to provide the higher level detail that is required for a study of this nature. Through the use of a time-dependent, three-dimensional, turbulent eddy-resolving method, the important time-varying, energy-containing turbulence structures within PSECs can be predicted allowing a detailed analysis of their mode of operation. This is achieved using large eddy simulation (LES) coupled with dynamic sub-grid scale (SGS) modelling that can provide accurate and reliable predictions of complex flows. Work on LES modelling of fluid flow through simpliefied PSEC goemtries, published by Khatir et al. (2016), reveals the need for complex modelling techniques to capture characteristic turbulence, while initial modeling trials by Theobald et al. (2018) highlight distinctions between single-phase and multiphase PSEC systems in their hydrodynamics. In the presented work, multiphase interface interactions are modelled using the volume of fluid (VOF) method with appropriate heavy and light phase fluidic properties capturing surface tension, density and viscous effects.

The simulations presented here were performed using the open source finite volume CFD code OpenFOAM® (Version 4.1).

2. Governing equations and simulation methodology

2.1. Fluid flow simulation approach

The large eddy simulation approach works on the basis of reducing the degrees of freedom of the flow problem through scale-separation of the flow domain. This is the removal of small-scale information that would otherwise be computationally expensive to resolve (energy scale filtering). Larger scales representative of the grid size can be calculated directly by solving the Naiver-Stokes equations. More precisely, the velocity fluctuations (turbulence) are calculated explicitly within the resolved scale field, defined by a cut-off length. Subsequently, the sub grid scales are modelled implicitly through the use of additional subgrid scale models. Typically, and especially for dynamic SGS models, the cut-off length is defined via mathematical filtering operations (Sagaut, 2010). A general definition for filtering is given by (Leonard, 1975):

$$\overline{U}(x,t) = \int G(r,x)U(x-r,t)dr \tag{1}$$

where the normalization condition is met when integrating over the entire flow domain and specified filter function G:

$$\int G(r,x)dr = 1 \tag{2}$$

and the velocity field is decomposed to the filtered velocity $\overline{U}$ and residual field u':

$$U(x,t) = \overline{U}(x,t) + u'(x,t) \tag{3}$$

The filtered mass and momentum equations in conservative form is then given by:

$$\frac{\partial \overline{U}_i}{\partial x_i} = 0 \tag{4}$$

$$\frac{d\overline{U}_j}{\partial t} + \frac{\partial \overline{U_i U_j}}{\partial x_i} = \nu \frac{\partial^2 \overline{U}_j}{\partial x_i \partial x_i} - \frac{1}{\rho}\frac{\partial \overline{P}}{\partial x_j} \tag{5}$$

the residual-stress tensor and turbulence kinetic energy, respectively, is given by:

$$\tau^R_{ij} = \overline{U_i U_j} - \overline{U_i}\,\overline{U_j} \tag{6}$$

$$k_r = \frac{1}{2}\tau^R_{ij} = \frac{1}{2}\overline{U_i U_j} - \frac{1}{2}\overline{U_i}\,\overline{U_j} \tag{7}$$

Provided the numerical mesh has been refined adequately, the approximated contributions from the SGS model should not dramatically impact the accuracy of the LES solution. However, given that a well-defined LES can have up to 20% of the energy spectrum modelled (80% resolved) it is still useful to consider the appropriateness of the SGS model available (Pope, 2000). In this case the LES was coupled with the dynamic Lagrangian SGS model from Meneveau et al. (1996). The dynamic Lagrangian SGS model is a variant of the Smagorinsky model. A Lagrangian temporal averaging approach is applied over fluid path-lines in order to calculate SGS model coefficients based on information from the larger unfiltered energy scales. This SGS model, therefore, incorporates considerations for the turbulence history of the case, in contrast to older and less accurate spatial averaging schemes that disregard such information. Although originally validated for systems with homogeneous directions it is readily applicable for unsteady flows with complex geometries, ideal for this study (Meneveau et al., 1996).

The dynamic Lagrangian SGS system of equations starts with decomposition of the residual stresses through double-filtering operations using *Germano's identity* (Germano, 1992):

$$T_{ij} = \widehat{\overline{U_i}\overline{U}_j} - \widehat{\overline{U}}_i\widehat{\overline{U}}_j = \widehat{\tau}^R_{ij} + L_{ij} \tag{8}$$

where the Leonard stresses (known as the 'resolved stresses') are:

$$L_{ij} = \widehat{\overline{U}_i\overline{U}_j} - \widehat{\overline{U}}_i\widehat{\overline{U}}_j = T_{ij} - \widehat{\tau}^R_{ij} \tag{9}$$

In the above equations the $\overline{()}$ represents single-filtering at length scale Δ and $\widehat{()}$ indicates double-filtering at length scale 2Δ. The LES simulations conducted in this research all used the length scale defined by the cell volume (V_C) as:

$$\Delta = C(V_C)^{\frac{1}{3}} \tag{10}$$

where the model coefficient C is taken as 1 (OpenCFD Ltd, 2016).

The framework of the Smagorinksy (1963) model is used to approximate the residual stresses from the Smagorinsky constant (c_s) and resolved rate-of-strain tensors ($\overline{S}_{ij}$ and $\widehat{\overline{S}}_{ij}$) using the model equations:

$$\tau^R_{ij} = -2c_s^2\Delta^2|\overline{S}|\overline{S}_{ij} \tag{11}$$

$$T_{ij} = -2c_s^2(2\Delta)^2|\widehat{\overline{S}}|\widehat{\overline{S}}_{ij} \tag{12}$$

together with a model equation for the scaled composite rate-of-strain tensor:

$$M_{ij} = 2\Delta^2\left[\widehat{|\overline{S}|\overline{S}}_{ij} - 4|\widehat{\overline{S}}|\widehat{\overline{S}}_{ij}\right] \tag{13}$$

For the model to dynamically consider turbulence evolution over time, C_s is evaluated at each time-step using:

$$C_s^2(x,t) = \frac{\mathscr{F}_{LM}}{\mathscr{F}_{MM}} \tag{14}$$

using the transport equations:

$$\frac{\partial \mathscr{F}_{LM}}{\partial t} + \frac{\partial}{\partial x_j}\overline{U}_j \mathscr{F}_{LM} = \frac{1}{\mathrm{T}}(L_{ij}M_{ij} - \mathscr{F}_{LM}) \tag{15}$$

$$\frac{\partial \mathscr{F}_{MM}}{\partial t} + \frac{\partial}{\partial x_j}\overline{U}_j \mathscr{F}_{LM} = \frac{1}{\mathrm{T}}(M_{ij}M_{ij} - \mathscr{F}_{MM}) \tag{16}$$

In this case, the relaxation time scale T, that is the memory length of the Lagrangian averaging, is taken as:

$$\mathrm{T} = \theta\Delta[\mathscr{F}_{LM}\mathscr{F}_{MM}]^{\frac{1}{8}} \tag{17}$$

with θ representing a dimensionless coefficient used for fine-tuning the model and time length of the Lagrangian averaging process (Meneveau et al., 1996). Typically $\theta = 1.5$, however for more complex industrial flows it is more appropriate to use $\theta = 3$, with the time scale increased to better capture historic turbulence effects of changing geometric properties of the flow along the fluid flow path-lines (Verma and Mahesh, 2012).

2.2. Multiphase modelling approach

The multiphase system was modelled using a one-fluid multiphase approach using the VOF method developed by Weller (2008) for OpenFOAM®'s 'interFoam' solver. In this case, mass and heat transfer were not considered. The motions of both incompressible immiscible fluids, i.e. the organic phase and aqueous phase liquids, are solved using a single set of momentum equations, mentioned previously. Surface tension (σ) is incorporated via an additional source term (F_s) added to the momentum equations

$$F_s = \sigma\kappa\frac{\partial \alpha}{\partial x_i} \tag{18}$$

computed from the curvature (κ) using

$$\kappa(x) = \frac{\partial n^f}{\partial x_j} \tag{19}$$

where n^f is the face centred interface normal vector.

The position of each fluid is tracked via the scalar field α representing the localised volume fraction. The aqueous phase liquid is represented when $\alpha = 1$ and the organic phase liquid is represented when $\alpha = 0$. Any intermediate value represents an immiscible mixture of the two fluids, particularly in regions of low mesh refinement. The time-dependent distribution of α for a LES is given by the transport equation:

$$\frac{\partial \alpha}{\partial t} + \frac{\partial}{\partial x_j}[\overline{U}_j\alpha] + \frac{\partial}{\partial x_j}[\overline{U}^r_j\alpha(1-\alpha)] = 0 \tag{20}$$

Here, any spatial variation in the fluids physical property, Φ, can be modelled and tracked through α using the weighting method:

$$\Phi = \alpha\Phi_{aq} + (1-\alpha)\Phi_{org} \tag{21}$$

In order to dampen numerical diffusion, the last term on the left-hand side of Eq. (20) is added to limit smearing of the interface via the relative artificial compression velocity U^r. The magnitude of numerical compression can be controlled via the user input variable C_α:

$$U_i^r = n_i^f min\left[C_\alpha\frac{|\phi_f|}{|s^f|}, max\left(\frac{|\phi_f|}{|s^f|}\right)\right] \tag{22}$$

where ϕ_f is the volumetric flux evaluated at the cell face surface and S^f is the cell face area vector. A more detailed breakdown of the specifics of the interFoam code is given by Deshpande et al. (2012). Typically $C_\alpha = 1$ is set as the default value when modelling free surface problems. However, for droplet dynamics it is more realistic to increase the level of compression to $C_\alpha = 4$, as shown by Tretola et al. (2017). Therefore, this modification was adopted in this simulation.

2.3. Computational domain and geometry

To best replicate industrial PSEC unit operations found in the nuclear reprocessing industry, the geometry used in this investigation was designed using generic sizing constraints taken from Logsdail and Slater (1991) in '*The Handbook of Solvent Extraction*' which provides a range of dimensions for previously operational PSECs. The dimensions of this column are listed in Table 1. Due to the complexities and varying length scales inherent to this geometry, a tetrahedral mesher was chosen to produce an unstructured three-dimensional purely tetrahedral mesh of 5.5 M nodes with refinement towards the plates and column walls, seen in Fig. 1.

The mesh in the near plate region was resolved in order to discretely capture droplet formation, droplet-fluid interactions and fluid transfer behaviour across the plate throughout pulsing. In order to reduce the computational burden, the mesh in the bulk flow region was resolved to a level high enough to accurately resolve enough of the turbulence energy spectrum and implicitly track the fluid motions of the dispersed phase fluid.

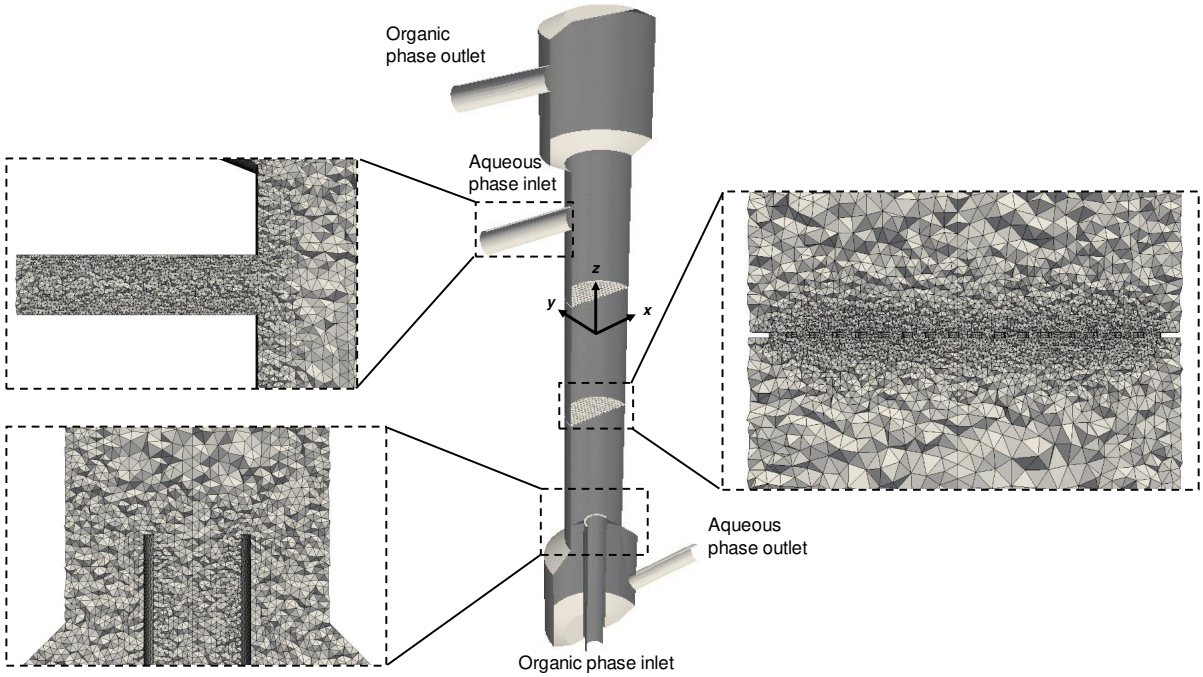

Figure 1: Geometry and mesh, with axis orientation, of PSEC used in CFD simulations.

Table 1: Characteristic dimensions of PSEC geometry

Parameter	Dimension
Column Diameter, D (m)	0.150
Column Height (m)	1.604
Decanter Heights (m)	0.300
Decanter Diameters (m)	0.250
Inlet / Outlet Diameters (m)	0.050
Number of Plates	2
Number of Holes	283
Hole Diameter, d (m)	4.46×10^{-3}
Fractional Free Area, e (%)	25
Plate Thickness (m)	0.002
Plate Spacing, h (m)	0.300
Bottom Inlet Height from Base (m)	0.350

More specifically, the volume of the largest tetrahedral cell, with edge length (l), is (2.016×10^{-7} m^3) which corresponds to an insphere radius of 2.44 mm comparable to the radius of the sieve-plate holes:

$$R = \frac{l}{\sqrt{24}} = \frac{\sqrt[3]{V_C 6\sqrt{2}}}{\sqrt{24}} \tag{23}$$

Furthermore, a two-plate geometry was chosen on the basis that the inter-compartmental hydrodynamics remain largely unchanged past the second plate. Similar reasoning has been used for justification of 2 - 4 plate models by previous investigators (Kolhe et al., 2011; Khatir et al., 2016). A large plate spacing of 300 mm was chosen in order to observe the inter-compartmental flow characteristics. A reasonable decanter height and diameter was chosen to provide enough fluid volume to dissipate agitative effects and allow for settling in these regions. The light phase inlet represents an ANSI schedule 80 pipe with a thickness of 5.54 mm.

2.4. Choice of operational parameters and fluid properties

To achieve a stable operation the inlet flow velocities and pulse velocity (Af), described in Section 2.5, were calculated using Eq. (24), from Smoot et al. (1959), and Eq. (25), from Berger and Walter (1985), which are both used to predict the throughput limit before flooding occurs $(U_c + U_d)_f$. Here, C_o is the orifice discharge coefficient taken as 0.6, a solvent-flow-ratio of 1 was chosen and C_t is the mass fraction of the solute in the aqueous feed. Since no mass transfer is included in this study C_t

is taken to be 0.

$$(U_c + U_d)_f = 0.527 \frac{\sigma^{0.144} \Delta\rho^{0.63} \mu_c^{0.489} H^{0.207} d^{0.458} g^{0.81}}{\rho_c^{0.775} \mu_d^{0.2} Q^{0.207}} \times \left(\frac{U_d}{U_c}\right)^{0.014} (Af)^{-0.621}$$
$$Q = \frac{\pi^2}{2C_o^2} \frac{1 - e^2}{e^2} \tag{24}$$

$$(U_c + U_d)_f = (24.528 + 2.537\sigma + 0.0548\sigma^2) \times (1 + 1.455e + 3.247e^2) \times \left[1 + 0.1778 ln \frac{U_c}{U_d} + 0.0437 \left(ln \frac{U_c}{U_d}\right)^2\right] \times (0.2115 D^{0.2} h^{0.18}) \left(1 + \frac{U_c}{U_d} \frac{h}{d} C_t\right)^{0.09} \tag{25}$$

Subsequently, the column was then characterised to be operating under a dispersed regime (between mixer-settler and emulsion regimes) using the pulse velocity transition limit (Af_t) calculated from Eq. (26) (Kumar and Hartland, 1983).

$$Af_t = \left[0.05\beta h \left(\frac{\rho_c}{\Delta\rho^{0.75} \sigma^{0.25} g^{1.25}}\right)^{-1}\right]^{\frac{1}{3}}$$
$$\beta = \frac{e^2}{(1 - e)(1 - e^2)} \tag{26}$$

$Af < Af_t$ Dispersion Regime

In this operational regime, the column produces stable mixing conditions forming clear dispersed organic phase droplets rising via gravity driven flow. More details of PSEC operating regimes and flooding is available in the paper '*Design aspects of pulsed sieve plate columns*' by Yadav and Patwardhan (2009).

With regards to the chemical properties, a tributyl phosphate (TBP)/dodecane mixture at 30/70 wt% and nitric acid were chosen as the light (organic) and heavy (aqueous) phase fluids respectively, with a surface tension of 9.83 mNm^{-1}. The density of TBP/dodecane and HNO_3 were taken as 806 kgm^{-3} and 1110 kgm^{-3} and the kinematic viscosities were taken as 2.35×10^{-6} and 1.017×10^{-6} m^2s^{-1} respectively.

2.5. Boundary conditions

A summary of the boundary conditions used are listed in Table 2. Conditions for the volume fraction, pressure, velocity and SGS model fields ($\mathscr{F}_{LM}, \mathscr{F}_{MM}, \nu_t$) were specified at the inlet, outlet and wall boundary patches as well as for the internal (initialised) field.

Inlet values for α were set according to the phase relevant at each boundary patch with a zero gradient condition (from cell centres to boundary faces) applied at the walls. The internal field for α was initialise to include a volume of organic fluid in the decanter zone at the top of the column, creating a droplet disengagement interface between the two fluids characteristic of PSECs. This was achieved by assigning any cell above a given reference height, in this case 1.3 m, $\alpha = 0$ and any cell bellow as $\alpha = 1$.

The OpenFOAM® interFOAM solver solves the momentum equation using a modified pressure field 'p_rgh', the static pressure excluding the hydrostatic contribution (calculated from the local cell density):

$$\text{p\_rgh} = P_{static} - \rho_{cell} g(h - h_{ref}) \tag{27}$$

This causes complications at the pressure boundary patches when modelling closed systems in instances where the density of the fluid varies significantly with height. In this case without modification, the pressure at the bottom (aqueous) outlet is overestimated as the hydrostatic head at that point is calculated based on the local heavier density and doesn't account for the lighter fluid in the disengagement section. In order to rectify this imbalance a custom condition was used:

$$P_{local} = P_0 - \rho_{cell}(1 - |U|^2) + \rho_{cell} g(h - h_{ref}) \tag{28}$$

This allows one to correctly assign considerations for the hydrostatic head contribution at each outlet via P_0 estimated through the expression:

$$P_0 = \rho_c g z_f - h_{ref} \tag{29}$$

where z_f is the z-direction cell-face-centre height and ρ_c is the density of the continuous phase in that region, namely nitric acid at the bottom outlet and TBP/dodecane at the top outlet. In both cases a reference height h_{ref} is used to discreetly set where there is a sharp change in density, i.e. at the disengagement interface.

A fixed velocity of 0.015 ms^{-1} was assigned for the aqueous phase inlet. In order to simulate pulsed dispersed flow, the organic phase inlet was prescribed by a time-varying sinusoidal boundary condition, available within the standard OpenFOAM® libraries, characterised as:

$$U = Af sin(2\pi f t) + U_{offset} \tag{30}$$

where the amplitude of the pulsation is controlled via A, the frequency of pulsation set by f and the mean velocity (average throughput) set by U_{offset}. Together, both

Table 2: Summary of boundary conditions used in simulation

Field	Heavy Phase Inlet	Light Phase Inlet	Heavy Phase Outlet	Light Phase Outlet	Wall	Internal Field
α	Fixed value 1	Fixed value 0	Outflow: Fixed gradient 0 Return flow: Fixed value 1	Outflow: Fixed gradient 0 Return flow: Fixed value 0	Fixed gradient 0	Non-uniform value
P_{local}	Fixed gradient corrected for velocity boundary	Fixed gradient corrected for velocity boundary	Customised condition 0	Customised condition 0	Fixed gradient 0	Uniform value 0
U	Fixed value (0, 0, 0.015)	Time-varying sine $A = 0.0125$ $f = 1$ $U_{offset} = 0.015$	Outflow: Fixed normal grad Return flow: Calculated from flu	Outflow: Fixed normal grad Return flow: Calculated from flu	No slip	Uniform value (0 0 0)
$\mathscr{F}_{LM}$	Fixed gradient 0	Fixed gradient 0	Fixed gradient 0	Fixed gradient 0	Fixed gradient 0	Uniform value 1×10^{-3}
$\mathscr{F}_{MM}$	Fixed gradient 0	Fixed gradient 0	Fixed gradient 0	Fixed gradient 0	Fixed gradient 0	Uniform value 1×10^{-3}
ν_t	Fixed gradient 0	Fixed gradient 0	Fixed gradient 0	Fixed gradient 0	Fixed gradient 0	Uniform value 0

conditions provide a solvent-flow-ratio of 1 and a total volumetric throughput of 0.106 m^3h^{-1}. The velocity at the outlets were given a mixed condition type. During normal outflow a zero gradient condition applies, whilst during events of return flow the incoming velocity is obtained from the flux in the patch-face normal component of the internal-cell value.

For the SGS transport equations, a value for the internal field must be set in order initialise the solution. However, these values are immediately overwritten and so are of little consequence to the final solution provided stable initial values are given.

2.6. Solution method

A transient Euler time-derivative scheme was used along with a multi-dimensional cell limited least-squares gradient scheme for all equations solved. Additionally, the velocity and volume fraction transport equations were solved using second-order divergence schemes. The SGS model transport equations were solved using a bounded first-order upwind divergence scheme, this is of particular necessity for this SGS model as unbounded scalars can quickly lead to divergence through negative values (Stoll and Porté-Agel, 2006). Convergence for the transient case was reached when the final residual fell below $1x10^{-6}$ for each transport equation at each time step. This was achieved using the transient PIMPLE (mixed PISO/SIMPLE) algorithm solving within 2 outer-loop iterations at each time step with 3 inner-loop iterations and with no under-relaxation, maintaining transient accuracy. Using the semi-implicit MULES (Multi-dimensional limiter with explicit solution) algorithm for descritsation of the volume fraction field, a fixed maximum Courant number was applied using an adjustable time-stepping option with the average Courant number oscillating between 0.006 and 0.012. An additional four inner-loop sub-cycling steps, through MULES, was also implemented to improve stability and accuracy of the solution of the volume fraction transport term. Final solutions were taken when time step convergence was observed, and the volume fractions and outlet velocities showed cyclic steady-state behaviour.

The simulation was parallelised and ran across 192 processors (~28,600 cells per processor) using the University of Leeds' ARC3 HPC facilities (University of Leeds, 2019). The time step was in the order of 0.0003 s once fully developed cyclic stead-state flow had been achieved. On average, a wall-clock time of 1.32 hrs produced 1 s of simulated transient flow.

2.7. Post-processing operations and analysis

In order to extract more information from the simulations than is generated directly by the solver, additional mathematical operations were performed in post-processing. To highlight persistent characteristics of the fluctuating flow field, results across 200 pulse cycles were ensemble time-averaged, denoted by $\langle\cdot\rangle$, into four sets of results at $1/2\pi$, π, $3/2\pi$ and 2π during the sinusoidal pulse cycle. From this, the mean velocity and pressure fields were calculated. Additionally, one can extract information on the turbulence kinetic energy from the velocity fluctuations, $U_i' = U_i - \langle U_i \rangle$, and resid-

ual sub grid contribution,

$$k_t = \frac{1}{2}\langle\overline{U_i' U_i'}\rangle + \frac{2}{3}\langle k_r\rangle \tag{31}$$

as well as, consequently, the 'turbulence resolution':

$$M = \frac{k_r}{\frac{1}{2}\langle\overline{U_i' U_i'}\rangle + k_r} \tag{32}$$

and the resolved field turbulence dissipation rate from the fluctuating rate-of-strain tensor and residual sub grid contribution:

$$\varepsilon = 2\nu\langle\overline{S_{ij}' S_{ij}'}\rangle + \langle\varepsilon_r\rangle \tag{33}$$

where the rate-of-strain tensor is defined as:

$$S_{ij} = \frac{1}{2}\left(\frac{\partial U_i}{\partial x_j} + \frac{\partial U_j}{\partial x_i}\right) \tag{34}$$

with

$$\varepsilon_r = \frac{C_\mu k_r^2}{\nu_t} \tag{35}$$

and the constant C_μ is taken to be 0.09 (Pope, 2004, 2000; Tennekes and Lumley, 1972). The total production of turbulence kinetic energy was calculated using Eq. (36). Both the mechanical production and buoyant flux terms were considered. Neglecting to include contribution from the buoyant flux term can result in a negative production of turbulence kinetic energy, an observed phenomena in multiphase flows (Gayen and Sarkar, 2011)

$$\begin{aligned}\text{Production of } k_t &= \begin{matrix}\text{Mechanical}\\ \text{production}\end{matrix} + \text{Buoyant flux}\\ &= -\langle U_i U_j\rangle\frac{\partial\langle U\rangle}{\partial x_j} + \delta_{i3}\frac{g_i}{\rho_c}\langle\rho' U_i'\rangle\end{aligned} \tag{36}$$

In order to determine the dispersive mixing capability, the 'mixing index' λ_{MI} field can be calculated from the magnitudes of the rate-of-strain tensor (shear-strain-rate), $|S|$, and vorticity tensor, $|\Omega|$. In this case, both where calculated from the filtered velocity field:

$$\overline{\lambda_{MI}} = \frac{|\overline{S}|}{|\overline{S}| + |\overline{\Omega}|} \tag{37}$$

where,

$$\Omega_{ij} = \frac{1}{2}\left(\frac{\partial U_i}{\partial x_j} - \frac{\partial U_j}{\partial x_i}\right) \tag{38}$$

The mixing index is a scalar variable used to quantify the ratio of rotational and irrotational flow components and is commonly used in industrial colloidal applications in assessing mixing effectiveness (Cullen, 2009). A value of 0 represents pure rotational flow, 0.5 represents simple shear flow, and value of 1 represents pure elongational flow. When irrotational flow is dominant, droplets experience a type of deformation which stretches (elongates) them inducing breakage and dispersion. Other modes of flow (rotational and shear) do not contribute as efficiently to dispersive mixing, instead inducing bulk or local rotation of the suspended droplets (Rauwendaal, 1999). Using this criteria, one can evaluate the dispersive mixing efficiency of the system *a priori* based purely on the velocity field. The mixing index field calculated from Eq. (37) was ultimately ensemble time-averaged for analysis.

Alternatively, other turbulence characteristics have been used to explain droplet breakup mechanisms in the formation of emulsions in turbulent flows. As described by Vankova et al. (2007), classical studies of emulsification theorise two modes of emulsification defined by the turbulent length scales and droplet sizes. When the size of the smallest turbulent eddies in the continuous phase are smaller than the droplets, deformation results under the action of pressure fluctuations and is known as the "turbulent inertial regime". When the smallest eddies are larger than the droplets viscous stresses inside and between the eddies result in deformation under the "turbulent viscous regime". Through comparison of the turbulent (Reynolds) stresses, Eq. (39), viscous stresses, Eq. (40) and eddy length scales, defined by the *Kolmogorov length scale* Eq. (41), the primary mode of mixing can be identified and used to describe mechanistically the functionality of PSEC mixing:

$$\tau_{ij}^t = \rho\langle U_i' U_j'\rangle \tag{39}$$

$$\tau_{ij}^v = 2\mu S_{ij} \tag{40}$$

$$\lambda_0 = (\nu_c^3/\varepsilon)^{1/4} \tag{41}$$

3. Results and discussion

3.1. Flow detail and turbulence resolution of the LES

Profiles of the magnitude of the instantaneous velocity fields are presented in Fig. 2. Shown here are two-dimensional slices across the y-normal plane ($x = 0$ m) at the end of the simulation at the four chosen characteristic points in the sinusoidal pulse cycle, the colour plot is presented on a logarithmic scale. From Fig. 2 it can seen that the LES was successful in capturing the time-dependent features of the velocity field at various length

scales throughout the flow domain. Notable characteristics in the flow include the large scale jet emerging from the organic phase inlet, the turbulent features in the organic inlet pipe and in those emerging before and after each sieve plate. The turbulence, facilitated by water entrainment, and buoyancy effects, from the influx of organic fluid, within the feed pipe obscure any observable time-dependent effects from the imposed velocity boundary condition. In each decanter zone, a sharp reduction in the flow velocity can be seen with development of the flow in the boundary regions. The flow entering the column from the aqueous phase inlet is mostly laminar/transitional in nature, with no sharp gradients in the velocity. The turbulent features observed in the organic inlet are a consequence of the multiphase interface interactions between the two fluids in that region, discussed further in Section 3.2.

The quality and accuracy of the LES was assessed using the resolution of the turbulence within the system. This was based on how much of the turbulence kinetic energy was explicitly resolved, from the velocity fluctuations, and what contributions were made from the SGS model. Fig. 3 shows a colour plot of the cell values of the turbulence resolution calculated using Eq. (32). The LES was found to resolve turbulence throughout the domain, with some individual cells under-resolved in the bulk flow region. However, a volumetric average showed only 2.6% of the turbulence energy spectrum is represented by the SGS model in this system, with the remaining resolved explicitly from the filtered LES, well above the recommended 80% resolution criteria (Pope, 2000, 2004). It was observed that close to the column wall boundaries and near the aqueous phase inlet k_r was likely overestimated. Large k_r contributions in the wall region are a consequence of the model which does not correctly consider scaling towards the wall; i.e.

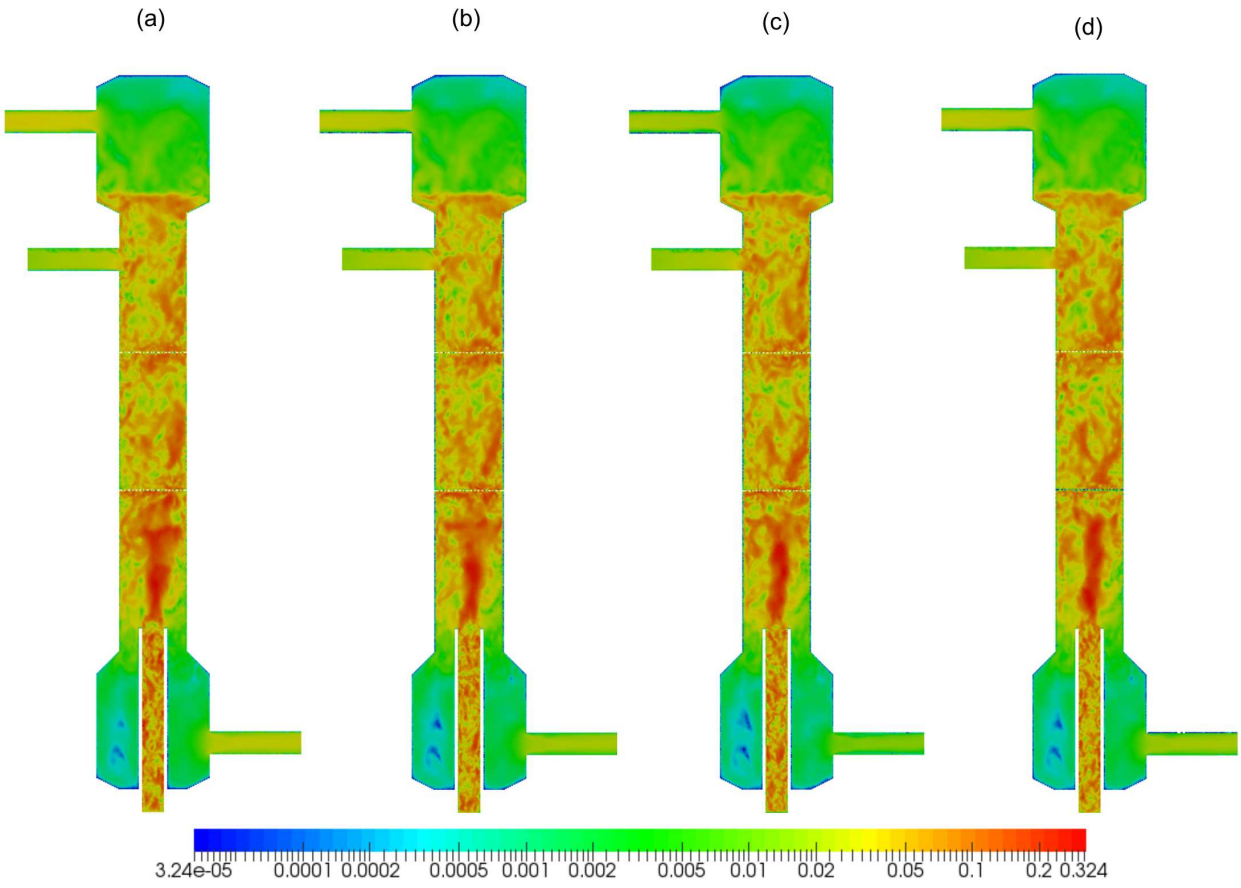

Figure 2: Magnitude of the instantaneous velocity field at (a) $\frac{1}{2}\pi$, (b) π, (c) $\frac{3}{2}\pi$ and (d) 2π. Velocities in ms^{-1}.

k_t should tend to zero at the wall. This was less of an issue in the plate region where the velocities, and therefore k_r, was explicitly resolved to the surface due to a high local mesh density. With regards to the aqueous phase inlet, the flow in this region is laminar/transitional due to low inlet velocity boundary condition. Consequently, k_r is likely to be over-contributing in this area also implying that the sub grid model employed may be less applicable at low Reynolds numbers. This could be avoided by increasing the grid resolution in these areas, however, it is of little consequence to the accuracy of the solution in the areas of interest.

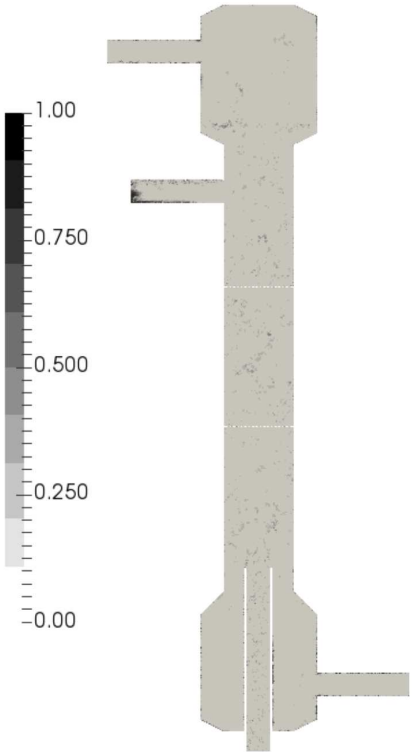

Figure 3: Plot of the LES turbulence resolution at $1/2\pi$.

3.2. Representation of the multiphase system

The time-dependent volume fraction of each fluid was tracked throughout the flow domain using the VOF method, a snap-shot of which has been provided in Fig. 4 at π. At the organic phase inlet the boundary condition was set to feed pure organic liquid ($\alpha = 0$). Here, the organic phase quickly coalesces into droplets through entrained aqueous liquid in the feed pipe, likely by way of surface tension and local turbulence effects. A small amount of organic liquid is also seen to entrain in the aqueous phase inlet pipe which reached an equilibrium amount after some time. This feature did not significantly influence development of the flow in the incoming aqueous phase feed.

The disengagement interface at the top of the column was seen to deviate and equilibrate +40 mm from its initial position. During typical operation, the level of this interface is managed to avoid carry-over during unstable operation. With severe flooding it is reported that hold-up tends to continuously deviate from equilibrium and the disengagement interface rises until carry-over eventually occurs (Mcallister et al., 1967).

The total hold-up of the system, which includes fluid in both the decanter regions, was found to equilibrate at 30.6 vol%, thus indicating stable (non-flooding) behaviour. Droplets were observed to form throughout the domain with little organic phase hold-up behind/under each plate, indicative of dispersion regime operation predicted by empirical correlations outlined in Section 2.4. The stage-wise equilibrium hold-up, from plate to plate at $z = 0.702 - 1$ m, was found to be low at 5.1 vol% despite running the column at a solvent-flow-ratio of 1. Industrial columns have run to hold-up values of 30 vol% before phase inversion occurs (Logsdail and Slater, 1991). The sinusoidal pulse caused the stage-wise hold-up to oscillate but by a small amount of $\approx \pm 0.1\%$. The extent of the stage-wise hold-up is important as it primarily dictates the extent of mass-transfer in the system, along with the hold-up distribution and interfacial surface area contact with the aqueous phase via the droplet-size distribution. Older laboratory experiments describe PSEC's running upto solvent-flow-ratios of 7 in order to achieve higher solvent loading (Lade et al., 2013). Solvent loading limitations highlight an obvious area for improvement in traditional PSEC designs and should be the focus of further research and development regarding process intensification of these units.

In regards to the numerical description and motion of the dispersed phase, a distinguishable level of numerical diffusion of α was observed in the bulk flow region despite the use of suggested numerical compression schemes and high mesh resolution. This is a consequence of the VOF method. Nevertheless, the general motion of droplet swarms between the plates were distinguishable in the bulk continuous phase flow and mechanisms of droplet formation can be seen above and across the plates. As for the near plate regions, droplets were observed to percolate through the plates continuously, detaching from the plate once enough fluid coalesced near a plate-hole to break surface tension and drive flow across. The VOF model used does not account for contact angle which may affect the wetting behaviour observed here.

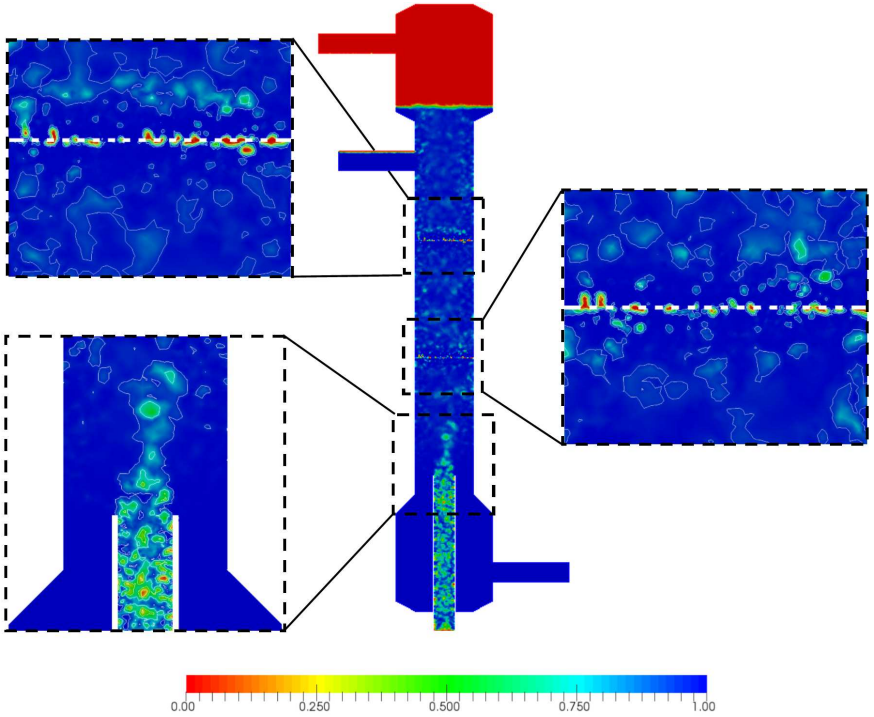

Figure 4: Plot of the instantaneous volume fraction field, α, at π. Contour lines have been plotted for reference at α values of 0.25, 0.5, 0.75 and 0.95.

3.3. Evaluation of hydrodynamics

Hydrodynamic behaviour was evaluated primarily from observation and predictions of the system's ensemble-averaged flow characteristics in terms of values of velocity, pressure, mixing index number, turbulence kinetic energy and turbulence kinetic energy dissipation rate. In doing so, persistent features of the flow can be evaluated.

Fig. 5 was generated by taking discrete values of the averaged velocity field across the column (x-axis at $y = 0$) at heights corresponding to the centre of the bottom plate ($z = 0.701$ m), the centre of the middle compartment ($z = 0.850$ m), and the centre of the top plate ($z = 1.001$ m) at each time considered. Continuous plots of the mean velocity components can be seen for predictions taken across the centre of the middle compartment. Discontinuous predictions across the plates are a result of the geometry, in that each curve is a prediction across a single hole with adjacent curves corresponding to adjacent holes. Due to the formation of large rotational structures between the plates, driven by gravitational effects, most of the momentum in the system is expressed largely in the z-direction with small rotational elements in the x and y directions. The flow in the centre of the compartment is seen to remain mostly invariant with regards to time with only small deviations in the flow structure. Conversely, the flow across each plate shows an observable evolution across the pulse cycle. At the maximum pulse amplitude (at $1/2\pi$) momentum in the positive (upward) z-direction is at its greatest and negative z-direction momentum is small, with the opposite observed at the minimum amplitude ($3/2\pi$). One might expect the flow to be comparable when the pulse cycle is at its median amplitude states, at π and 2π. However, a slight preference in the positive z-direction is observed at 2π compared with that at π. Nevertheless, the variations observed across the plate, with respect to time, are relatively small despite the fact that the pulse velocity is comparable to the mean feed velocity.

With respect to the spatial distribution of momentum across the bottom plate, a persistent positive peak in the z-direction is observed in the flow with small negative peaks towards the edge of the plate (where $x > \pm 0.05$ m). This is indicative of the large pulsing jet from the organic phase inlet impinging on the bottom plate. At this point, the organic phase is distributed across the plate and the surrounding continuous phase flow (under the plate) separates into two large vortices either side of the jet. This also indicates that during this mode of operation (dispersed regime) there is an uneven transfer of

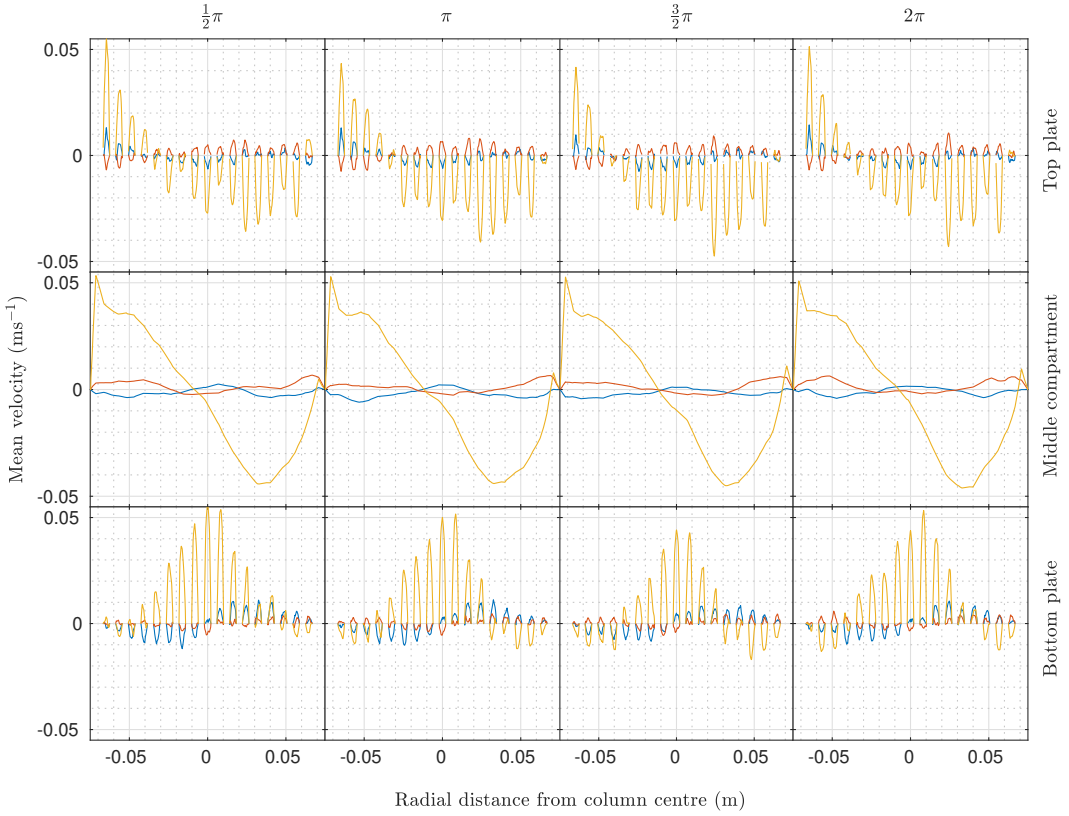

Figure 5: Ensemble averaged mean velocity components plotted along the x-axis (y= 0 m) at z= 0.701 m (centre bottom plate), z= 0.850 m (middle of the compartment), z= 1.001 m (centre of top plate) at $\frac{1}{2}\pi$, π, $\frac{3}{2}\pi$ and 2π; $\langle U_x \rangle$ (—), $\langle U_y \rangle$ (—), $\langle U_z \rangle$ (—).

fluids across the plate, with the continuous phase more likely transferring across, in the downward direction, at the outer edges of the plate.

The continuous phase flow in the centre of the middle compartment was observed to be dominated by a large rotational structure, in the y-normal plane, encompassing the entire volume of the compartment. This is represented in Fig. 5 by the distribution of the mean velocity across the column, with a clear upward momentum for $x < 0$ m and downward momentum for $x > 0$ m. Without quantitative historical (Lagrangian) tracking of the droplets un-available in the VOF model is it unclear how such structures affect the path and residence time distribution of the droplets in the column. However, the droplets were observed to more likely transit across the compartment where $x < 0$ m. Such behaviour will hinder the extraction efficiency during mass transfer operations due to the creation of artificial concentrations of the solvent droplets on one side of the column. Moreover, the continuous phase fluid is likely to stagnate within the rotational structure increasing residence time which would effect the equilibrium concentration of the solute within the column.

The rotational structure observed in the middle compartment clearly influences the flow across the top plate, resulting in a similar distribution of the z-direction momentum. This is likely a consequence of the resulting path of the droplets before reaching the plate. Assuming this behaviour persists in a PSEC with more stages, this could have serious implications for the efficiency of the system in terms of solute-solvent contact, discussed previously, and flow resistance across the plate. Systems which exhibit flow resistance across the plates could be more sensitivity to flooding having a lower maximum throughput capacity, in which case it would be advisable to introduce downcommers and other plate features in order to control the distribution of the dispersed phase and improve transfer paths of each fluid across the plates. The hydrodyamics of such design features in PSECs have been briefly explored by Yadav and Patwardhan (2009).

The ensemble-averaged pressure ($P_{static} - \rho gh$), turbulence kinetic energy , turbulence kinetic energy dissipation rate, and mixing index were calculated along

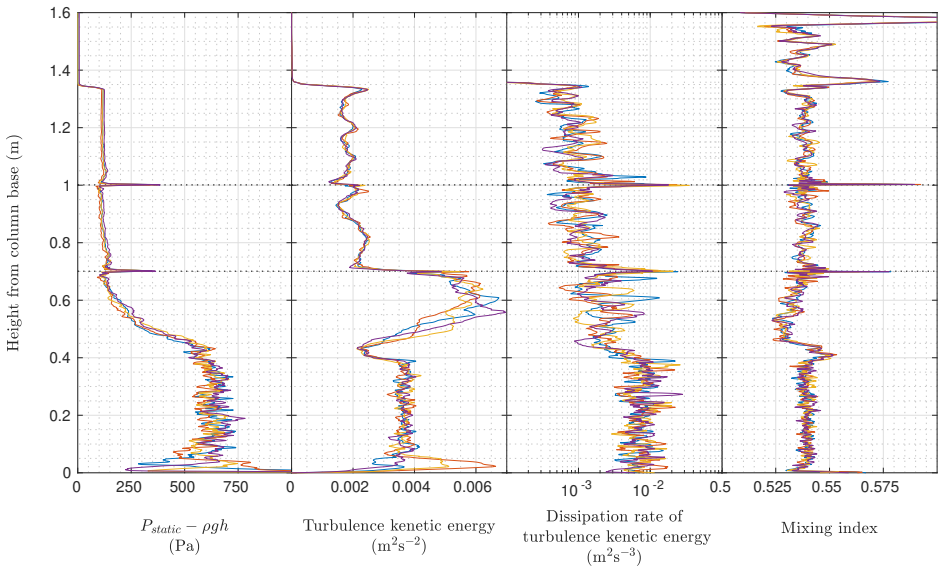

Figure 6: Field properties plotted along the height of the column at x= 0 m, y= 0 m; $\frac{1}{2}\pi$ (), π (), $\frac{3}{2}\pi$ (), 2π ().

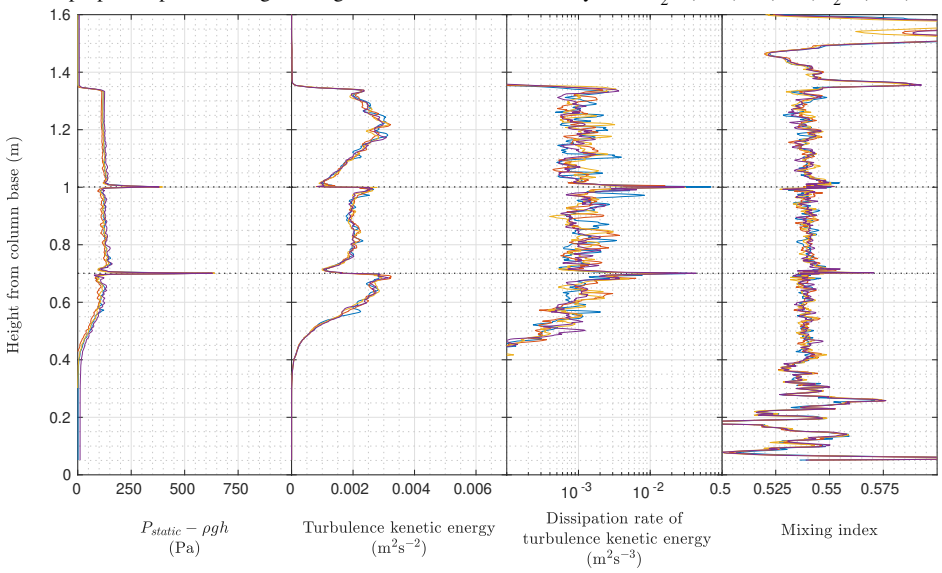

Figure 7: Field properties plotted along the height of the column at $x = -0.05$ m, $y = 0$ m; $\frac{1}{2}\pi$ (), π (), $\frac{3}{2}\pi$ (), 2π ().

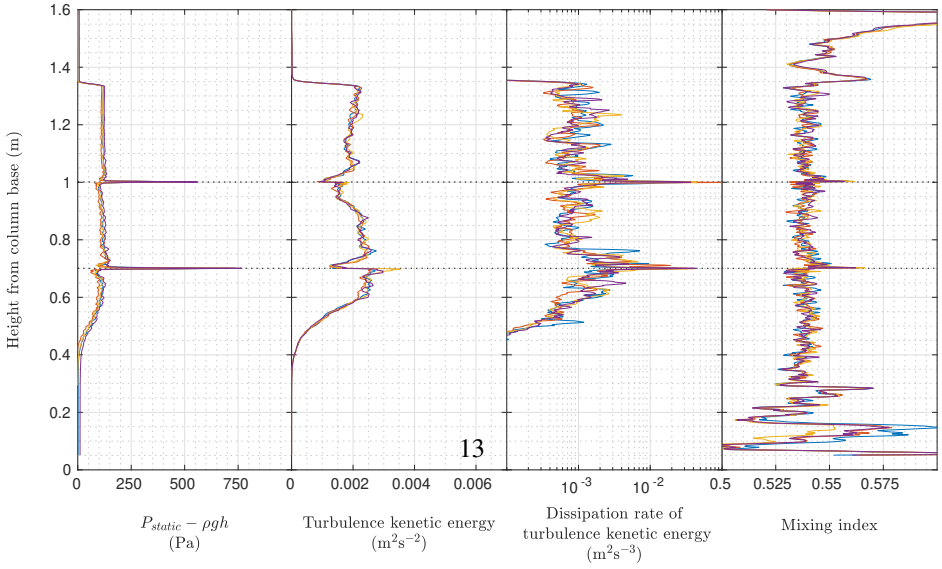

Figure 8: Field properties plotted along the height of the column at $x = 0.05$ m, $y = 0$ m; $\frac{1}{2}\pi$ (), π (), $\frac{3}{2}\pi$ (), 2π ().

the z-axis at x= 0 m, x= −0.05 m, and x= 0.05 m, all at y= 0 m with the results presented in Fig. 6, Fig. 7, and Fig. 8 respectively. In each case, plots of the flow properties highlight notable characteristic behaviour at the plates and proportionally little variation with respect to time, with the exception being the turbulence kinetic energy dissipation rate at the plates.

Fig. 6 shows that the organic phase enters the column at high pressure, with respect the rest of the column. The velocity of the fluid and buoyancy effects in the confined pipe region lead to a relatively high velocity and, therefore, a high dynamic pressure contribution which is quickly damped on exit of the inlet pipe (at z = 0.4 m). Even after averaging, there is still a significant level of spatial fluctuation in the pressure gradient within the organic inlet pipe, this feature also being observable in plots of the turbulence properties. This suggests that the flow in this region is particularly dynamic and turbulent despite having an assigned low Reynolds number velocity condition at the boundary. Variations in the local density from droplet formation and buoyancy effects are likely driving the creation of turbulence in this region. This observation is of particular importance for those implementing RANS models wherein the turbulent conditions must be assigned at the boundary. One may assume rather laminar conditions, but the observations here suggest this is clearly not the case.

Between the organic phase inlet and the first plate (0.4 m <z< 0.7 m) the pressure quickly normalises, as mentioned before, to a stable operating dynamic pressure ≈ 120 Pa. This pressure is roughly maintained throughout the column, although large pressure spikes observed across each plate. More specifically, there is a pressure spike, drop, and recovery across each plate. This is a consequence of *Bernoulli's principle* and conservation of mass across the sieve-plate, which is expected behaviour in a choked flow (Yadav and Patwardhan, 2009). Comparing pressure results between the centre of the column, Fig. 6, and close to the walls, Fig. 7 and Fig. 8,the pressure between the plates is comparable (little variation with radial distance), although the pressure spike across the sieve-plates is greater towards the walls than in the centre of the column. Similar patterns are also apparent in the turbulence kinetic energy dissipation rate. The uneven distribution of pressure and turbulence kinetic energy dissipation rate across each plate is likely a consequence of the uneven velocity distribution, seen in Fig. 5.

The turbulence kinetic energy of the system at x= 0 m is seen to increase towards the bottom plate then quickly drop off as the pulsing jet of organic fluid passes through the plate. The organic phase below the bottom plate accelerates, as a result of buoyancy, with this and impingement on the plate resulting in a gain in turbulence kinetic energy. This is then quickly dampened at the first plate suggesting that the overall distribution of the organic fluid is inefficient with regards to desired mass transfer performance. Subsequently, the level of turbulence kinetic energy remains approximately constant throughout the rest of the column, and roughly constant with regards to radial distance, although with a slight increase and then drop and recovery through the top plate. The level of turbulence kinetic energy dissipation rate is also shown to be approximately equal throughout the bulk flow regions of the column with some notable spikes through the plates. Again, comparing Fig. 6 to Fig. 7 and Fig. 8 it is evident that more dissipation occurs towards the walls of the column than in the centre line.

The quality of dispersive mixing in the system was determined using the mixing index value which quantitatively assesses the types of flow inherent within the system. Fig. 6, Fig. 7 and Fig. 8 all indicate the system is principally characterised as a simple shear flow with all values of the index between 0.5 − 0.6. An average value of 0.54 is consistent along the height of the working section of the column (0.4 m < z < 1.3 m) with some slight improvement across the plates. Macroscopically, this means that the system is poor at producing the types of flow that are thought to contribute to the breakup of droplets as discussed in Section 2.7. This also suggest that in order to improve the performance of these columns more consideration should be given to the plate design and manipulation of the resulting flow structure to promote elongational flow.

Additionally, the turbulence characteristics were further assessed in relation to their impact on mixing. Namely, in terms of the comparative contributions of the turbulent to viscous stresses, the turbulence length scales, turbulence kinetic energy and budget terms in the production and dissipation of turbulence kinetic energy.

Classical discussion of PSECs, in particular in Yadav and Patwardhan (2008), mention 'shear forces' as directly responsible for the determination of droplet size/hold-up and, by extension, the column operational regime. Moreover, shear forces are said to result from the sieve-plate geometry and spacing. It is unclear whether the authors are describing viscous, turbulent or the total shear in the system, stresses, often used as a synonym to describe shear indirectly, or the individual shear components of the stress tensor or some other mathematical description relating to shear. In this study, the magnitude of the viscous and turbulent stress tensors

were calculated and compared, the aim being to understand mechanistically how PSECs accomplish mixing. Fig. 9 compares the turbulent stresses, arising from fluctuations in fluid momentum, and viscous stresses, resulting from a fluids resistance to physical deformation.

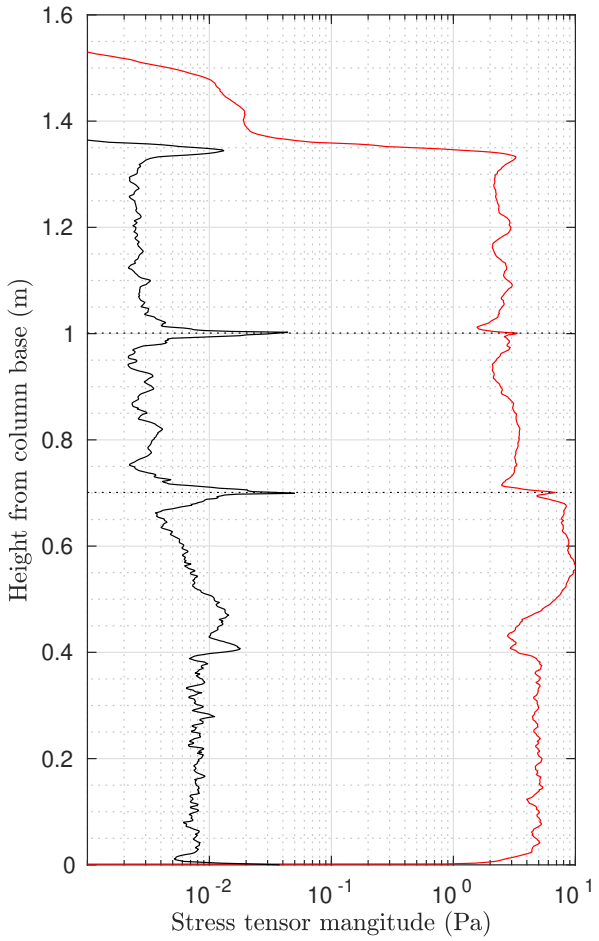

Figure 9: Magnitudes of the viscous (—) and turbulent stress (—) plotted along the height of the column at 2π.

Firstly, the turbulent stresses within the system are three orders of magnitude greater than the viscous stresses. Consequently, these results illustrate that turbulence has the greatest influence on PSEC operation. Secondly, although the viscous stresses are influenced by the sieve-plates, increasing by an order of magnitude in the near-plate region, the dominant turbulent stresses show no direct relationship with the plate (i.e. no increase near the plate). The turbulent stresses do show a slight increase and drop before and after the sieve-plate however, a result of the turbulence kinetic energy changes in these regions observed in Fig. 6, Fig. 7 and Fig. 8. Thirdly, the size of the smallest eddies were calculated to be 1.68×10^{-4} m, an order of magnitude smaller than the droplets observed evolving from the sieve-plate, as can be seen in Fig. 4. The eddie size was calculated using Eq. (41) with an estimated a dissipation rate of 0.0013 m^2s^{-3} taken from averaging dissipation rates given in Fig. 6 between both plates (0.702 m $< z <$ 1.002 m). Eddies within the plate sieve-holes, where the dissipation rate spikes, will be even smaller. As mentioned in Section 2.7, the Kolmogorov length scale can be used to determine if mixing occurs due to turbulence or viscous influences (Vankova et al., 2007). Here, the length scale indicates that mixing is performed under a turbulent inertial regime further justifying the hypothesis that the turbulent stresses are predominately responsible for mixing in PSECs.

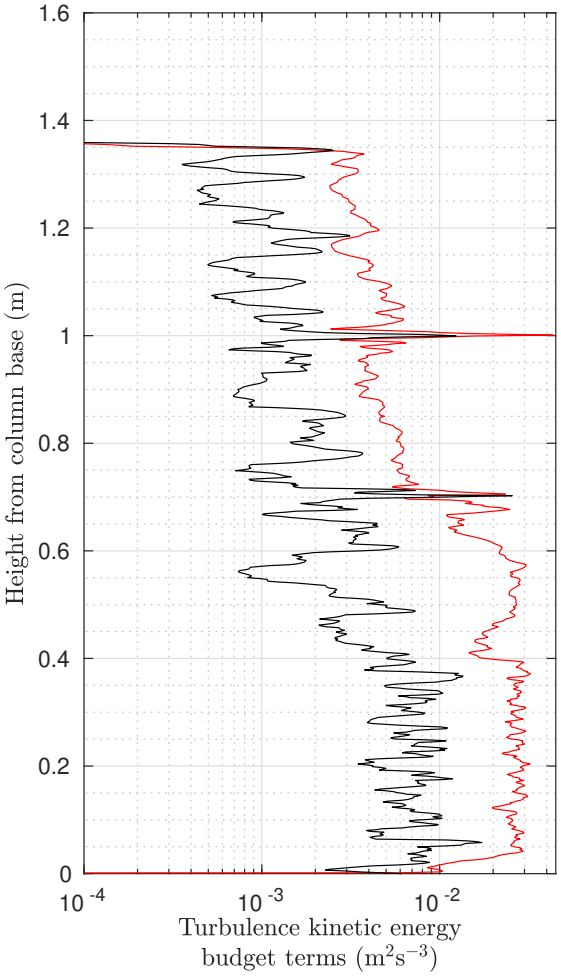

Figure 10: Disspation rate (—) and total production (—) of turbulence kinetic energy plotted along the height of the column at 2π.

In contrast to the previous points, a number of studies have shown sieve-plate geometry and spacing to directly influence PSEC operating behaviour (Yadav and Patwardhan, 2008). Rather than this being explained through viscous (shear) effects in the near-plate region, the evidence presented here suggests that sieve-plate design may instead have a direct relationship with the production, dissipation and resulting kinetic energy within the system, and therefore with the operation of PSECs. Fig. 10 compares the total production, see Eq. (36), and dissipation of turbulence kinetic energy along the height of the column. In both plots there are clear increases through the sieve-plates indicating that the plates do influence the turbulence in these regions. However, both terms are relatively balanced which would explain why no significant increase was observed in the turbulent stresses near the plates. Moreover, the difference between the production and dissipation terms in the bulk flow drops after the first plate resulting in less turbulence kinetic energy throughout the rest of the system. Consequently, the turbulence potential available for mixing thereafter is dampened due to the design of the first plate. Eq. (41) describes the minimum size of the turbulence length scale, and therefore mixing performance, to be inversely proportional to the dissipation rate. Therefore, improvement to sieve-plates capacity to produce turbulence kinetic energy would, in-turn, facilitate increases in the dissipation rate in the bulk flow and likely improve mixing throughout the system.

4. Conclusions

Presented here are the conclusions from a numerical investigation concerning the hydrodynamic characteristics of a PSEC representative of those found in nuclear reprocessing industries. Evidence was presented to show the column operating in a pseudo steady-state dispersed regime, via available design correlations, and analysis and assessment of the predictions from the LES coupled VOF CFD model are as follows:

1. During dispersed regime operation the macroscopic fluid flow properties were found to show time-invariance despite a prescribed sinusoidal pulsing condition at the organic phase inlet boundary.
2. For dispersed regime PSECs, turbulence was found to be the biggest contributing hydrodynamic factor to dispersive mixing determined through direct comparison of viscous and turbulent stresses.
3. The PSEC sieve-plate design used in this study, based on traditional designs, was found to be ineffective for the distribution and facilitation of turbulence for mixing which directly influences the size and stability of dispersed phase immiscible droplets.
4. Analysis of the decomposed turbulence kinetic energy budget suggests improvements to the plate design could be made to preserve the dissipation rate throughout the column, via greater turbulence production at the plates, resulting in smaller droplets in the bulk flow region improving mass transfer.
5. Assessment of the mixing index criteria also highlights that classic square-edge round-hole sieve-plate designs are poor at generating the types of (elongational) flow that contribute to the breakup of droplets in turbulent flow, therefore reducing the efficiency of turbulent mixing.
6. The stage-wise organic phase hold-up for the PSEC design considered was found to be low, at 5.1 vol%, when operating at a solvent-flow-ratio of 1.
7. Although stable non-flooding operation was achieved in the simulation, the resulting flow structures showed observable restriction in the near-plate regions and non-homogeneous distribution of droplets between the plates.
8. The LES was successful in producing time-dependent information of the hydrodynamics to a high resolution capturing the majority of the turbulence energy spectrum.

This study highlights the importance of time-dependent three-dimensional flow modelling in understanding the intricacies of PSEC operation. Further studies are required to compare the presented results against previously explored Reynolds-averaged predictive approaches and two-fluid multiphase flow models. Quantified validation of the LES-based PSEC model against experimental data is also necessary, although at the present time there is a paucity of data that could be used in this regard.

5. Acknowledgements

The authors thank the UK's EPSRC and the GENIORS research consortium for funding the research described. This research is part of the GENIORS project which has received funding from the Euratom research and training programme 2014-2019 under Grant Agreement No 7555171.

References

Berger, R., Walter, K., 1985. Flooding in pulsed sieve plate extractors. Chemical Engineering Science 40, 2175 – 2184.

Cullen, P.J., 2009. Food Mixing: Principles and Applications. Wiley.

Deshpande, S.S., Anumolu, L., Trujillo, M.F., 2012. Evaluating the performance of the two-phase flow solver interFoam. Computational Science and Discovery 5.

Gayen, B., Sarkar, S., 2011. Negative turbulent production during flow reversal in a stratified oscillating boundary layer on a sloping bottom. Physics of Fluids 23.

Germano, M., 1992. Turbulence: the filtering approach. Journal of Fluid Mechanics 238, 325.

Khatir, Z., Hanson, B.C., Fairweather, M., Heggs, P.J., 2016. High-fidelity CFD simulations of pulsed sieve-plate extraction columns, in: ETMM11, White Rose Uniersity Consortium, Palermo.

Kolhe, N.S., Mirage, Y.H., Patwardhan, A.V., Rathod, V.K., Pandey, N.K., Mudali, U.K., Natarajan, R., 2011. CFD and Experimental Studies of Single Phase Axial Dispersion Coefficient in Pulsed Sieve Plate Column. Chemical Engineering Research and Design 89, 1909–1918.

Kumar, A., Hartland, S., 1983. Correlations for dispersed phase holdup in pulsed sieve-plate liquid-liquid extraction columns. Chemical Engineering Research and Design 61, 248–252.

Lade, V.G., Rathod, V.K., Bhattacharyya, S., Manohar, S., Wattal, P.K., 2013. Comparison of normal phase operation and phase reversal studies in a pulsed sieve plate extraction column. Chemical Engineering Research and Design 91, 1133–1144.

Leonard, A., 1975. Energy Cascade in Large-Eddy Simulations of Turbulent Fluid Flows. Advances in Geophysics 18, 237–248.

Logsdail, D., Slater, M., 1991. Pulsed Perforated-Plate Columns, in: Lo, T.C., Baird, M.H.I., Hanson, C. (Eds.), Handbook of Solvent Extraction. Krieger Publishing Company, Florida, pp. 355–457.

Mcallister, R.A., Groenier, W.S., Ryon, A.D., 1967. Correlation of flooding in pulsed, perforated-plate extraction columns. Chemical Engineering Science 22, 931–944.

McKetta, J.J., 1998. Encyclopedia of Chemical Processing and Design: Volume 65 – Waste: Nuclear Reprocessing and Treatment Technologies to Wastewater Treatment: Multilateral Approach. Chemical Processing and Design Encyclopedia, Taylor & Francis, Boca Raton.

Meneveau, C., Lund, T.S., Cabot, W.H., 1996. A Lagrangian dynamic subgrid-scale model of turbulence. Journal of Fluid Mechanics 319, 353–385.

OpenCFD Ltd, 2016. OpenFOAM User Guide. Technical Report. Bracknell.

Pope, S.B., 2000. Turbulent Flows. Cambridge University Press, Cambridge.

Pope, S.B., 2004. Ten questions concerning the large-eddy simulation of turbulent flows. New Journal of Physics 6.

Rauwendaal, C., 1999. New dispersive mixers based on elongational flow. Plastics, Additives and Compounding 1, 21–23.

Sagaut, P., 2010. Large Eddy Simulation for Incompressible Flows: An Introduction. Scientific Computation. 2nd ed ed., Springer Berlin Heidelberg, Berlin.

Sen, N., Singh, K.K., Patwardhan, A.W., Mukhopadhyay, S., Shenoy, K.T., 2018. CFD simulations to predict dispersed phase holdup in a pulsed sieve plate column. Separation Science and Technology (Philadelphia) 00, 1–14.

Smagorinksy, J., 1963. General circulation experiments with the primative equations. Monthly Weather Review 91, 99–164.

Smoot, L.D., Mar, B.W., Babb, A.L., 1959. Flooding characteristics and separation efficiencies of pulsed sieve plate extraction columns. Industrial and Engineering Chemistry 51, 1005–1010.

Stoll, R., Porté-Agel, F., 2006. Dynamic Subgrid-Scale Models for Momentum and Scalar Fluxes in Large-Eddy Simulations of Neutrally Stratified Atmospheric Boundary Layers Over Heterogeneous Terrain. Water Resources Research 42, 1–18.

Tennekes, H., Lumley, J.L., 1972. A First Course in Turbulence. The MIT PRess, Massachusetts.

Theobald, D.W., Hanson, B., Fairweather, M., Heggs, P., 2018. Multiphase Large Eddy Simulation of a Pulsed Sieve-Plate Extraction Column, in: Waste Management Symposia, Phoenix, Arizona, US. pp. 1–15.

Tretola, G., Vogiatzaki, K., Navarro-Martinez, S., 2017. Detailed simulation of air-assisted spray atomization: effect of numerical scheme at intermediate Weber number, in: 28th conference on liquid atomization and spray systems, pp. 6–8.

University of Leeds, 2019. Advanced research and computing, ARC3.

Vankova, N., Tcholakova, S., Denkov, N.D., Ivanov, I.B., Vulchev, V.D., Danner, T., 2007. Emulsification in turbulent flow: 1. Mean and maximum drop diameters in inertial and viscous regimes. Journal of Colloid and Interface Science 312, 363–380.

Verma, A., Mahesh, K., 2012. A Lagrangian subgrid-scale model with dynamic estimation of Lagrangian time scale for large eddy simulation of complex flows. Physics of Fluids 24, 85101.

Weller, H., 2008. A new approach to vof-based interface capturing methods for incompressible and compressible flow. Technical Report. OpenCFD Ltd.

Yadav, R.L., Patwardhan, A.W., 2008. Design Aspects of Pulsed Sieve Plate Columns. Chemical Engineering Journal 138, 389–415.

Yadav, R.L., Patwardhan, A.W., 2009. CFD Modeling of Sieve and Pulsed-Sieve Plate Extraction Columns. Chemical Engineering Research and Design 87, 25–35.